Magnons in disordered nonstoichiometric low-dimensional magnets

Paweł Buczek,[1,2] Leonid M. Sandratskii,[1] Nadine Buczek,[1] Stefan Thomas,[1,*] Giovanni Vignale,[2] and Arthur Ernst[1]
[1]*Max Planck Institute of Microstructure Physics, Weinberg 2, 06120 Halle (Saale), Germany*
[2]*Department of Physics and Astronomy, University of Missouri, 223 Physics Building, Columbia, Missouri 65211, USA*
(Received 1 March 2016; revised manuscript received 5 July 2016; published 2 August 2016)

We study spin excitation spectra of one-, two-, and three-dimensional magnets featuring nonmagnetic defects at a wide range of concentrations. Taking the Heisenberg model as the starting point, we tackle the problem by both direct numerical simulations in large supercells and using a semianalytic coherent-potential approximation. We consider the properties of the excitations in both direct and reciprocal spaces. In the limits of the concentration c of the magnetic atoms tending to 0 or 1 the properties of the spin excitations are similar in all three dimensions. In the case of a low concentration of magnetic atoms the spin excitation spectra are dominated by the modes confined in the real space to single atoms or small clusters and delocalized in the reciprocal space. In the limit of c tending to 1, we obtain the spin-wave excitations delocalized in the real space and localized in the reciprocal space. However, for the intermediate concentrations the properties of the spin excitations are strongly dimensionality dependent. We pay particular attention to the formation, with increase of c, of the Lorentzian-shaped peaks in the spectral densities of the spin excitations, which can be regarded as magnon states with a finite lifetime given by the width of the peaks. In general, low-dimensional magnets are more strongly affected by the presence of nonmagnetic impurities than their bulk counterparts. The details of the electronic structure, varying with the dimensionality and the concentration, substantially influence the spin excitation spectra of real materials, as we show in the example of the FeAl alloy.

DOI: 10.1103/PhysRevB.94.054407

I. INTRODUCTION

The spin excitations (SEs) in magnets with reduced dimensionality, including wires and thin films, attract strong interest from the experimental, theoretical, and applied physics perspective. Impressive experimental progress, in particular the inelastic scanning tunneling microscopy [1,2] and spin-polarized electron energy loss spectroscopy (SPEELS) [3–5], allows us to probe directly their properties.

The low-dimensional magnets are often imperfect and feature deviation from the stoichiometry as well as disorder caused by alloying and doping, diffusion (intermixing) processes, the presence of contaminants during the preparation, and many more. These features result in the absence of the translational invariance and, in general, the SEs cannot feature the Bloch-like (spin-wave) character typical for perfect crystals. However, under certain conditions, one still anticipates the existence of well-defined extended spin-wave states, which can be pictured as Bloch waves with a finite lifetime arising from the scattering on the crystal imperfections. This picture of damped spin waves might break down if the spectra become dominated by strongly spatially localized modes. The understanding of the spin-wave formation and their damping is of great theoretical and practical importance. The damping mechanism, which is strongly pronounced in metallic magnets, involves the interaction of the spin waves with single-particle spin-flips called Stoner excitations [6,7] and is referred to as Landau damping. It has been shown that contrary to earlier predictions [8], the Landau damping does not necessarily increase with the reduced dimensionality [9,10]. In this paper we consider completely different aspects of the formation and damping of spin-wave excitations, i.e., we address the impact of nonstoichiometric concentration of the magnetic atoms and their spatial disorder.

We will refer to the systems composed from magnetic and nonmagnetic atoms or vacancies as *magnetic-nonmagnetic alloys* (MNAs). In three dimensions, there exist numerous important MNA systems, including recently discovered ultrastrong low-density steels based on FeAl alloys [11]. The characterization of their magnetic properties, including SE spectra, is important from the point of view of prospect applications. Also the class of diluted magnetic semiconductors has been extensively investigated [12–15] in the context of their employment in spintronic devices. Recently, Qin *et al*. demonstrated that in the 2D magnetic system, ultrathin Fe films on Pd, one can substantially lengthen the lifetime of spin waves by reducing the Landau damping [5]. It is achieved by means of a band structure engineering, i.e., adding nonmagnetic atoms into the magnetic film. Also examples of imperfect one-dimensional magnetic nanowires exist [16], which makes important the study of the properties of the SEs in one-dimensional systems.

Chakraborty *et al*. addressed the magnon spectra of three-dimensional disordered magnets [15,17,18] using a self-consistent local random phase approximation [19]. The same method was used to study lifetime effects of magnons in two-dimensional magnetic systems [20]. However, little is known about the properties of magnetic excitations in disordered magnets as their dimensionality changes from three dimensions (bulk) to two (films) and to one (wires). SE spectra can be studied using time-dependent density functional theory combined with the coherent-potential approximation (CPA). Unfortunately, such studies exist only for bulk systems [21,22]. Up to now, there are no studies allowing us to assess the performance of the CPA in the description of SEs in disordered media by comparing the approximation to an exact result. In this paper, our starting point for studying SEs is the adiabatic

*Corresponding author: sthomas@mpi-halle.mpg.de

spin dynamics based on the mapping of the magnetic states of the magnets onto the states of the Heisenberg Hamiltonian [23]. This approach neglects Landau damping, which allows us to separate clearly the influence of the nonstoichiometry and disorder on the magnon lifetime from other dissipation mechanisms.

We consider here only the uncorrelated disorder, as defined in Sec. II B. Even under this simplifying assumption, the classical Heisenberg model of randomly distributed interacting ferromagnetic spins with arbitrary concentration of magnetic atoms cannot be solved analytically and we tackle this problem from two complementary perspectives. First, we resort to the direct diagonalization of the Heisenberg Hamiltonian in the real space and subsequent statistical averaging of relevant quantities, in particular the magnetic susceptibility, which carries information about the SE spectra [24], over different possible disordered configurations of magnetic atoms. A similar strategy for three-dimensional disordered magnets was adopted in Ref. [17]. Because the configurations are sampled pseudorandomly we refer to this method as "Monte Carlo." While this method is numerically exact, it is computationally expensive. As a possibility to overcome this difficulty, we developed an approximate analytic solution to the model, which is based on the coherent-potential approximation. Due to the presence of off-diagonal disorder [25,26], the CPA is formally much more involved for the Heisenberg Hamiltonian than for the electronic problem [27]. Therefore, only simple cases of binary alloys with primitive three-dimensional lattices were studied up to now [28–30]. In this paper we generalize the CPA to incorporate complex unit cells with arbitrarily many types of impurity atoms.

The paper is organized as follows. In Sec. II we outline the formalism for describing the SEs and our model of disordered nonstoichiometric magnetic systems. Following this, we evaluate the spectra of SEs of the model based on either the direct diagonalization or the coherent-potential approximation. In Sec. III we consider disordered magnets in different dimensions to study the impact of dimensionality on the SE spectrum. The performance of the coherent-potential approximation is evaluated. Finally, in Sec. IV we investigate how the realistic electronic structure influences the properties of imperfect magnets, studying FeAl alloy at different Al concentrations in three and two dimensions.

II. FORMALISM

A. Description of spin excitations

The adiabatic spin dynamics approximates a magnetic system with the classical Heisenberg Hamiltonian of interacting magnetic moments located on lattice sites

$$\mathcal{H} = -\frac{1}{2}\sum_{pr} J_{pr}\mathbf{e}_p \cdot \mathbf{e}_r, \tag{1}$$

where $p,r,\ldots$ label the sites, $\mathbf{e}_p$ is the direction of the moment on the site p, and J_{pr} are the so-called exchange parameters. In the case of ferromagnets the energetically lowest excitations of this Hamiltonian are spin excitations involving small-amplitude precessions of the moments around the direction of the ground-state magnetization. Their properties are described by the retarded transverse magnetic susceptibility $\chi_{pr}(\omega + \mathrm{i}0^+)$ (0^+ stands for an infinitesimal positive quantity) [10]. The susceptibility gives the amplitude of the precession of the magnetic moment on the site p around its ground-state direction upon applying oscillating magnetic field on the site r with frequency ω and direction transverse to the ground-state magnetization.

The susceptibility can be represented as

$$\chi = gGS, \tag{2}$$

where g is the electron g factor, which we assume to be equal to 2 in this work, and G and S are matrices in the space of atomic sites. S is a diagonal matrix

$$S_{pr} = S_p\delta_{pr}, \tag{3}$$

where S_p is the spin moment at the site p and G is the *magnon spin propagator*

$$G(z) = G_0(z) + G_0(z)gSTG, \tag{4}$$

$$G_0(z) = \mathsf{I}z^{-1}, \tag{5}$$

where z stands for the complex frequency, I is the unit matrix, G_0 is the *free spin propagator*, and the *torque matrix* T is defined as

$$(ST)_{pr} = S_r^{-1}\delta_{pr}\sum_l J_{pl} - S_r^{-1}J_{pr}. \tag{6}$$

Equation (5) can be formally solved by the matrix inversion

$$G^{-1} = G_0^{-1} - gST, \tag{7}$$

which allows us to compute the susceptibility for any frequency using Eq. (2). The evaluation of the magnetic susceptibility of the disordered nonstoichiometric magnets of different dimensions is the main theoretical tool employed in this paper, since this quantity directly yields the spectrum of the SEs.

The anti-Hermitian part of the susceptibility

$$\mathcal{L}\chi(\omega + \mathrm{i}0^+) = \frac{1}{2\mathrm{i}}[\chi(\omega + \mathrm{i}0^+) - \chi(\omega + \mathrm{i}0^+)^\dagger], \tag{8}$$

where $\chi^\dagger$ stands for the Hermitian conjugate of the susceptibility, is called the *loss matrix*. It is particularly useful in the description of SEs [10]. Its eigenvalues yield the spectral density of the excitations at the given energy ω and the corresponding eigenvectors give the spatial form of the excitations.

B. Model of disorder

In this work we consider the substitutional disorder. Magnetic and nonmagnetic atoms of different types randomly occupy the sites $\mathbf{R} + \mathbf{s}_i$ of a periodic crystal, where $\mathbf{R}$ are the vectors of the Bravais lattice and i labels the positions of the basis sites in the primitive cell. The dimensionality of the lattice is arbitrary. Atomic types are denoted with Greek letters $\alpha,\beta,\ldots$. We define the *occupation function* $p^\alpha(\mathbf{R} + \mathbf{s}_i)$, which is 1 if the site $\mathbf{R} + \mathbf{s}_i$ is occupied by the atom of type α and 0 otherwise. Some sites might be not occupied giving rise to vacancies. To simplify the notation we define $p^{\alpha i}(\mathbf{R}) \equiv p^\alpha(\mathbf{R} + \mathbf{s}_i)$.

If the energy of the mixture depends only weakly on the relative positions of atoms, the fact that the site p is occupied

by the atom α does not influence the occupation of the neighbor site r and we speak about *uncorrelated disorder*. The model of uncorrelated disorder is widely adopted in the studies of metallic alloys and, as mentioned in the introduction, the correlation effects are neglected in this study. The uncorrelated disorder is fully specified by the probability $c_{i\alpha}$ of finding an atom of the type α on the basis site i.

C. Direct numerical averaging

The magnetic susceptibility can be readily computed for a finite fragment of an infinite crystal by means of the direct inversion of the $|z - gST$ matrix. In parallel to this real-space technique, it is useful to consider the Fourier transformation of the susceptibility, since this quantity can be directly probed in a scattering experiment, e.g., SPEELS [31] or STM [2]. We consider a supercell featuring periodic boundary conditions, so that the Fourier transformation of the susceptibility

$$\chi_{ij}(\mathbf{q},\mathbf{q}') = \sum_{\mathbf{R}\mathbf{R}'} \mathrm{e}^{-\mathrm{i}\mathbf{q}\cdot\mathbf{R}} \mathrm{e}^{\mathrm{i}\mathbf{q}'\cdot\mathbf{R}'} \chi(\mathbf{R}+\mathbf{s}_i,\mathbf{R}'+\mathbf{s}_j) \qquad (9)$$

is defined for discrete values of the wave vectors $(\mathbf{q},\mathbf{q}')$ from the first Brillouin zone consistent with the size of the supercell. Again, i and j label the basis sites. The pair of indices $i\mathbf{R}$ specifies the particular crystal site p. The frequency argument is suppressed for brevity.

The atomic occupation of the sites in the supercell is chosen randomly according to the probabilities $c_{i\alpha}$. Each concrete realization of the atomic arrangement in the supercell is called a *configuration*. The susceptibility is computed for numerous different configurations (typically between 100 and 1000) and subsequently averaged. We sample the configurations by means of pseudorandom numbers and thus refer to this method as Monte Carlo. The standard deviation of the mean is computed in order to prove the convergence with respect to the number of samples. In addition, the cells of growing size are considered in order to eliminate the influence of the finite-size effects.

A single random configuration of atoms does not in general feature the translational symmetry of the underlying lattice. However, the averaging described above restores this symmetry such that the average susceptibility $\langle\chi(\mathbf{R},\mathbf{R}')\rangle$ depends only on the difference $\mathbf{R}-\mathbf{R}'$ between the lattice vectors of the primitive cells. This in turn implies that only the diagonal terms of the Fourier-transformed susceptibility with $\mathbf{q}=\mathbf{q}'$ become nonzero:

$$\langle\chi_{ij}(\mathbf{q},\mathbf{q}')\rangle = \Omega_{\mathrm{BZ}}\delta(\mathbf{q}-\mathbf{q}')\langle\chi_{ij}(\mathbf{q})\rangle \qquad (10)$$

$$\approx N\delta_{\mathbf{q}\mathbf{q}'}\langle\chi_{ij}(\mathbf{q})\rangle. \qquad (11)$$

Here, Ω_{BZ} is the volume of the first Brillouin zone. The latter approximation is valid for supercells containing N primitive cells, and

$$\langle\chi_{ij}(\mathbf{q})\rangle = \frac{1}{N}\sum_{\mathbf{R}\mathbf{R}'} \mathrm{e}^{-\mathrm{i}\mathbf{q}\cdot(\mathbf{R}-\mathbf{R}')} W\langle\chi(\mathbf{R}+\mathbf{s}_i,\mathbf{R}'+\mathbf{s}_j)\rangle. \qquad (12)$$

D. Coherent potential approximation

The coherent-potential approximation [27] allows us to compute the statistical average (12) approximately but in a numerically efficient semianalytic manner, without the necessity of working in the real space with large supercells and thus inverting large matrices. Its formulation for a MNA ferromagnetic Heisenberg model on a simple three-dimensional lattice was given by Matsubara [25] and is based on earlier works by Matsubara and collaborators (see references in paper [25]). A detailed discussion of the account for the off-diagonal disorder in the study of the electronic properties was given by Blackman *et al.* [26]. The electronic off-diagonal disorder corresponds to the random intersite hopping parameters that has close mathematical analogy to the random interatomic exchange parameters of the Heisenberg model. A number of later studies [28–30] refer to the electronic CPA by Blackman *et al.* as the basis of their developments on the CPA for the Heisenberg spin Hamiltonian. Although the implementations of the method by different authors differ in details, the foundations of all works on Heisenberg-CPA are similar. In the Appendix, we follow the derivations by Matsubara and Yonezawa, generalizing the CPA formalism to the case of complex crystals featuring multiple sites in the primitive cell, arbitrary number of atomic species forming the disordered alloy, and arbitrary dimensionality.

If we restrict ourselves to the first term in the expansions (A21) and (A22) we obtain the so-called *virtual-crystal approximation* (VCA). This approximation replaces a nonstoichiometric disordered system with a periodic one with the value of the exchange parameter weighted by the concentration of the magnetic atoms. The VCA was widely used in the past to provide a crude picture of the magnetic spectrum in disordered magnets. It is a very convenient approximation, since it requires no self-consistency and the corresponding self-energies and weight correction are energy independent. Unfortunately, as we will see later, the VCA fails qualitatively to account for several important properties of magnon spectra in low-dimensional disordered magnets.

The VCA leads to the non-physical picture, in which atoms of different types are allowed to *simultaneously* occupy the same atomic site. The CPA approximately but systematically takes into account the "exclusion effects" [27], which guarantee that for a particular atomic configuration every site is occupied by one particular atom only. The CPA results in an energy-dependent self-energy, which defines an effective uniform (periodic) medium. Its imaginary part gives rise to the finite lifetime of magnetic excitations. We note also that the self-energy is not only dynamic but also wave-vector dependent (nonlocal), unlike the self-energy in the electronic structure CPA formalism [32]. The reason for that is the nonlocal character of the interaction: the role of the local on-site electronic potential is assumed by the nonlocal torque matrix T.

In the case of a local interaction, the CPA has several physical interpretations, among them the one that the effective medium is chosen in such a way that single-site fluctuations relative to it do not on average lead to any scattering. No such intuitive picture seems to exist in the Heisenberg model case, since it is not intuitively clear how the scattering from a nonlocal potential should be understood. However, as proven by Yonezawa [27] this intuitive condition is equivalent to the noncrossed cumulant expansion and in the construction of the CPA for this type of models one can still follow this formal path.

III. DIMENSIONALITY TRENDS: MODEL STUDY

From the point of view of nanoengineering it is of great importance to investigate how defects in a magnetic system, i.e., the presence of vacancies or nonmagnetic atoms in the otherwise magnetic lattice, influence the spectrum of magnetic excitations in different dimensions.

Nonstoichiometry and atomic disorder influence the SE spectrum in two different ways. On one hand, they alter the electronic structure resulting in the change of the values of atomic moments and the strength of the exchange coupling constants. On the other hand, even if these quantities were not affected, the change in the occupation of atomic sites must influence the properties of the SEs. In this part of our study, we consider a simple model of an imperfect magnet in order to disentangle the impact of the electronic structure and the geometry on the properties of spin waves in magnets in different dimensions.

In three dimensions, we consider a cubic lattice with the constant a. Every lattice point features six nearest neighbors. In two dimensions we choose a single (001) plane. The corresponding lattice is quadratic with the coordination number four and the distance between nearest neighbors a. The one-dimensional (100) nanowire counterpart involves lattice points in a distance a from each other with two nearest neighbors. In any dimension, each lattice point can be either occupied by a magnetic moment S or be empty (nonmagnetic). The concentration of magnetic atoms is given by c so that $c = 1$ corresponds to a perfect periodic structure and $c = 0$ denotes an empty lattice. We assume that in any dimension only nearest neighbors are magnetically coupled by the exchange parameter J, which depends neither on the dimensionality nor on the concentration of imperfections.

Despite these simplifications the model outlined above has an important property in the context of this study. In the case of a perfect magnet ($c = 1$), the magnons with wave vectors along the (100) direction Γ-X have the dispersion $\omega_{\mathbf{q}} = 4gJa^{-1}\sin^2(q)$, which does not depend on the dimensionality. [A similar relationship exists for two and three dimensions and the direction (110).] Furthermore, the spin-wave stiffness constant D for the perfect magnets is equal in all three dimensions to $D = gaJ$. In what follows we assume $a = 1$ and $J = (4g)^{-1}$ so that $D_1 = \frac{1}{4}$. Using this property we can easily assess the impact of imperfections on the spin-wave energies and lifetimes as a function of dimensionality and reveal pertinent trends. In Sec. IV we will drop these simplifying assumptions to recover the impact of the CPA *ab initio* electronic band structure on the spin-wave spectra of disordered alloys for different dimensionalities.

The Monte Carlo technique described in Sec. II C is employed in Secs. III A and III C to investigate the properties of spin-wave spectra in general and in the long-wavelength regime, respectively. In Sec. III B the applicability of the CPA and VCA approaches to study the properties of magnons in disordered magnets will be assessed.

A. Spin excitation spectra

An example of a one-dimensional random structure of the type considered in this work is presented in Fig. 1. The structure was generated by placing magnetic atoms on a site with probability $c = 0.7$. Any magnetic atom interacts at most with two nearest neighbors, which leads to the splitting of the structure into separate clusters of different sizes. We vary the number N_s of sites in the system in order to estimate and exclude the finite-size effects. Figure 2 presents spin-wave spectra for the wave vector $(0.25,0,0)2\pi/a$ and systems of different sizes. The spectra correspond to the imaginary part of the susceptibility $-\frac{1}{\pi}\mathrm{Im}\langle\chi(\omega+\mathrm{i}\gamma,\mathbf{q})\rangle$ averaged over N_c different, randomly generated atomic configurations. The limiting case of $N_c = 1$ is also considered and corresponds to the susceptibility of one particular configuration.

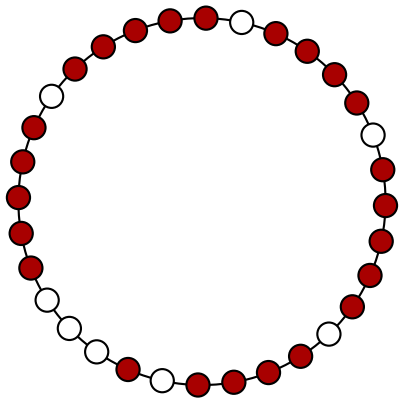

FIG. 1. Example of one-dimensional MNA with 32 sites and periodic boundary conditions. The structure was generated by placing the magnetic atoms (filled red circles) on a site with probability $c = 0.7$. Any magnetic atom interacts at most with two nearest neighbors.

The most pronounced feature of the spectra is the presence of a series of sharp SEs with the linewidth induced only by the artificial broadening $\gamma = 10^{-2}$. The corresponding localized modes emerge in the separate atomic clusters of different sizes, which are formed in the structure; cf. Fig 1. The different height (intensity) of the peaks is a consequence of the different number of states with the particular energy as well as of the value of the overlap integral between the particular SE and the plane wave with the wave vector $\mathbf{q}$.

As expected, the number and intensity of peaks depend on the size N_s since for larger systems more different types of atomic clusters of varying sizes (and, in higher dimensions, shapes) emerge; please compare Figs. 2(a) and 2(b). For large enough systems the spectra become weakly dependent on the size, which signifies that the distribution of cluster sizes within one single realization of the magnetic system practically approaches the thermodynamic limit; cf. Fig. 2(c). Finally, as evident from Fig. 2(d), the limit can be also reached for much smaller clusters but upon averaging over many different atomic configurations.

In our model of MNAs, the magnetic atoms interact only with the nearest neighbors, which makes the model affine to the problem of site percolations [33]. The percolation threshold c_p is the critical value of the occupation probability, above which a connected cluster of occupied sites spanning the entire system emerges. In one dimension any value of $c < 1$ leads to a split of the structure into separate clusters of different

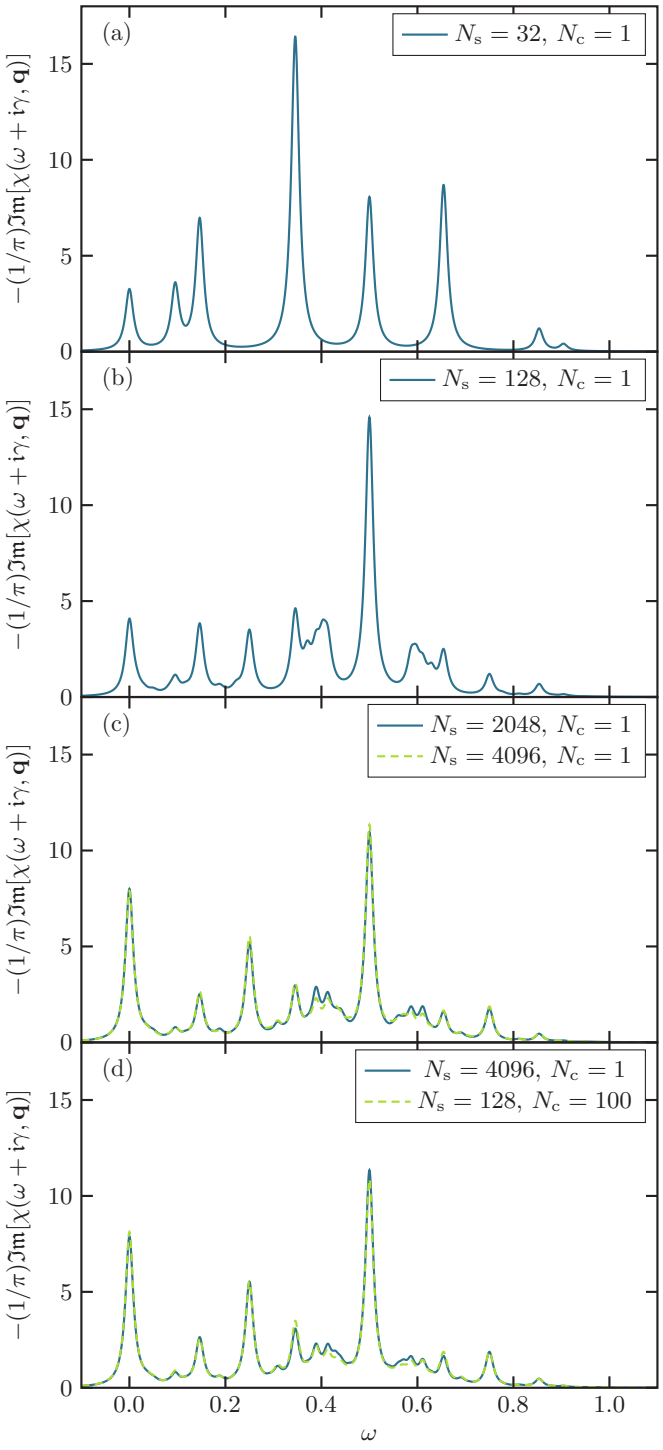

FIG. 2. Spin-wave spectra for a one-dimensional random MNA and the wave vector $(0.25,0,0)2\pi/a$. Atomic sites are occupied by a magnetic atom with the probability $c = 0.7$. Systems of different sizes N_s and averaging over different number of random configurations N_c are considered. The artificial broadening $\gamma = 10^{-2}$ was applied. The spectrum corresponding to the structure depicted in Fig. 1 is presented in panel (a).

sizes, while for square and simple cubic lattices in two and three dimensions c_p amounts to about 0.59 [34] and 0.31 [35,36], respectively. Reference [36] reports values 0.25 and 0.20 for body-centered and face-centered cubic structures, respectively. Figure 3 presents examples of two-dimensional uncorrelated MNAs at concentrations well below, around, and above the percolation threshold. The emergence of large connected clusters of interacting magnetic atoms has, as will be shown below, a profound impact on the spectra of magnetic excitations.

It must be stressed that the clusters arise randomly and are not driven by any attracting interaction as considered in Ref. [18].

Figure 4 shows the evolution of the SE spectra as the dimensionality of the disordered magnets is varied. While the spectra in one dimension are composed of sharp peaks corresponding to localized standing SEs, the two- and three-dimensional magnets above the percolation threshold feature *continua* of the SE states for a given wave vector; i.e., the SE peaks feature intrinsic finite widths. The continua form due to the presence of many excited states close to each other in energy. Because of the presence of the disorder the wave vector $\mathbf{q}$ ceases to be a good quantum number of the individual SE. From the physical point of view the broadened SE peaks can be treated as SEs with a finite lifetime. As evident from Fig. 5 the impact of the nonstoichiometry and disorder decreases with increasing dimensionality, as the lattices in higher dimensions are generally better connected resulting in lower values of c_p. Indeed, in three dimensions we obtain well-formed, relatively narrow magnon peaks at lower concentrations of magnetic atoms.

Figure 5 presents selected spectra for a larger wave vector in different dimensions. Comparing Figs. 4(b) and 5(b) we notice that well-defined narrow Lorentzian-like peaks are in general obtained for small wave vectors only, similar to the case of Landau damping in materials such as bcc Fe [10]. The example of the spectrum in Fig. 5(c) shows that the region in the Brillouin zone, in which single well-formed SE peaks are obtained, increases with the dimensionality.

Below the percolation threshold the localized SEs become strongly pronounced again, due to the formation of small detached islands; cf. Fig. 6.

We remark that the concentration of magnetic atoms above c_p does not mean that finite atomic islands cannot form at all. The spectrum in Fig. 5(b) still features, in addition to the continuum of delocalized SEs, sharp peaks with energies 0, 0.25, and 0.5 corresponding to such small islands not connected to the extensive atomic clusters spanning large areas of the crystal. We can quantify the contribution of these islands to the spectrum of magnetic excitations. The detached clusters feature necessarily only a few standing SE modes, among them the Goldstone mode, i.e., the mode with the vanishing frequency. Because of the finite spatial localization, the latter mode appears in the spectra for any wave vector $\mathbf{q}$, contrary to perfect crystals, in which it is seen only for $\mathbf{q} = \mathbf{0}$. Therefore, we can use the intensity (area under the peak) $I_0(c)$ of this zero-energy feature to estimate the influence of the detached islands on the magnetic excitation spectrum. In order to allow easy comparison, we normalize the intensity to the concentration of the magnetic atoms, $I_0(c)/c$. In perfect crystals, $c = 1$, this quantity assumes the value of $2S$, where S is the atomic magnetic moment, for $\mathbf{q} = \mathbf{0}$, and is zero otherwise. For MNAs, it differs from zero in the entire Brillouin zone. It approaches the value of $2S$ for any wave

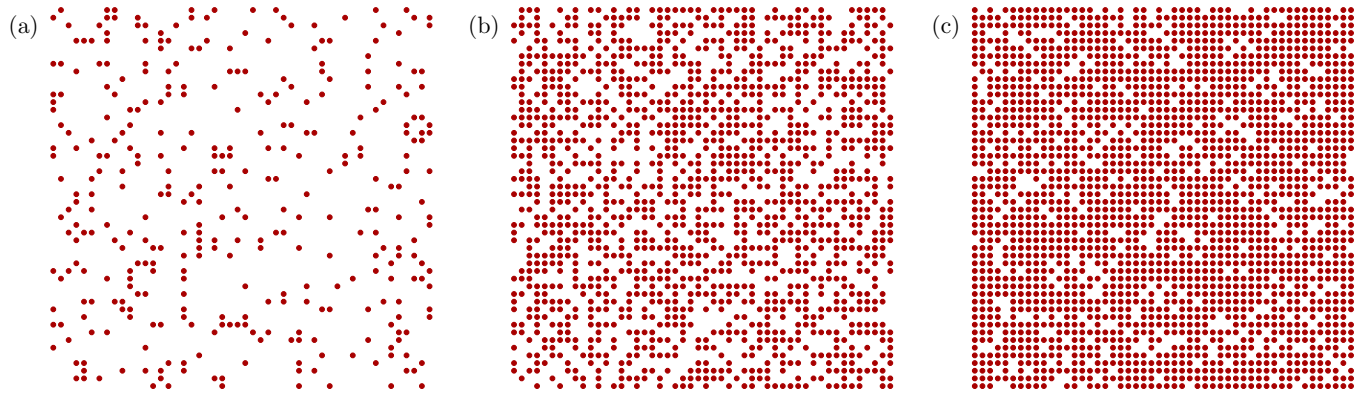

FIG. 3. Two-dimensional uncorrelated magnetic-nonmagnetic mixtures at different concentrations of magnetic atoms: (a) diluted limit at $c = 0.15$, (b) at the percolation threshold $c_p = 0.59$, and (c) in the dense limit $c = 0.85$.

vector in the limit of small concentrations. In this regime, practically only single, not-connected magnetic atoms appear in the system. We recall that such single atoms have only one resonant mode of the vanishing energy. The evolution of $I_0(c)/c$ for $\mathbf{q} = (0.25,0,0)2\pi/a$ as a function of concentration in different dimensions is presented in the Fig. 7. There are two important conclusions that follow from the analysis of Fig. 7. First, for any concentration, the zero-energy peak is

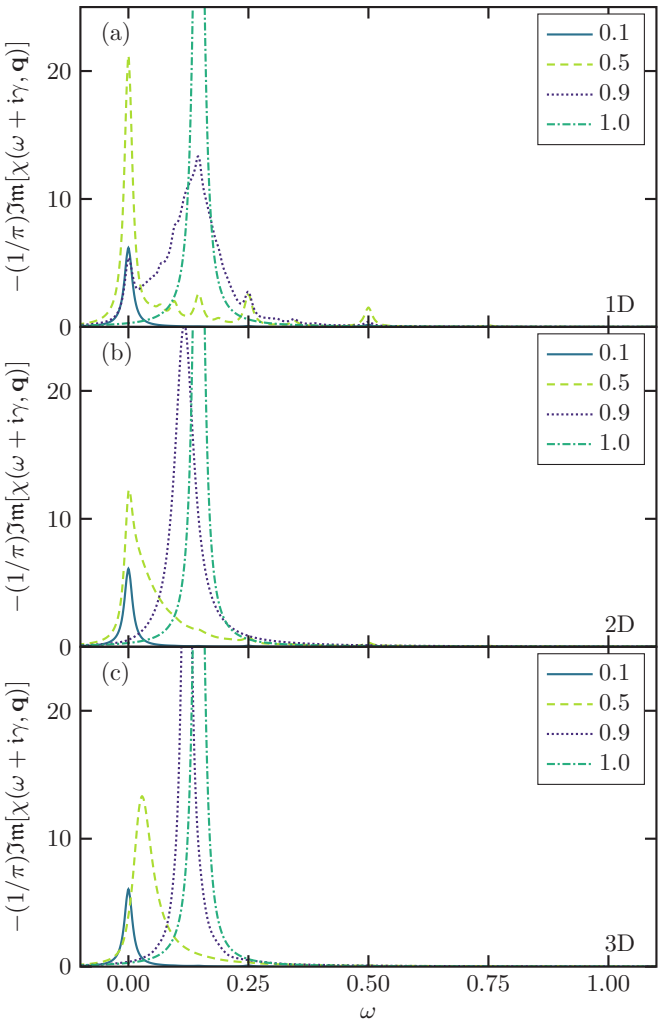

FIG. 4. Spin-wave spectra for random MNAs in different dimensions, the wave vector $(0.125,0,0)2\pi/a$, and different concentrations. The artificial broadening $\gamma = 10^{-2}$ was applied.

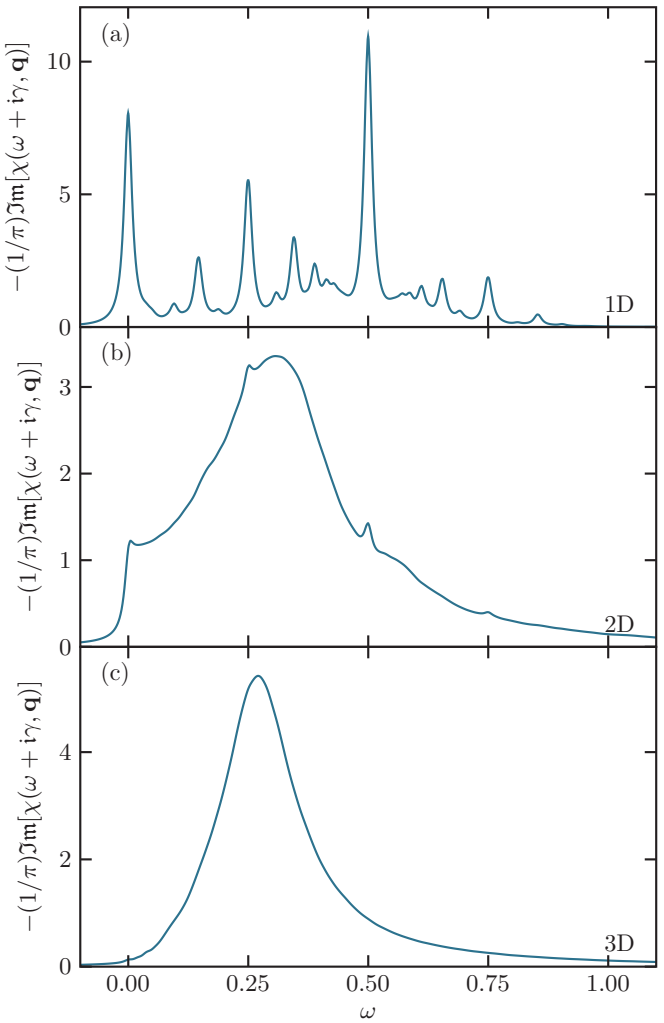

FIG. 5. Spin-wave spectra for random MNAs in different dimensions, the wave vector $(0.25,0,0)2\pi/a$, and the concentration $c = 0.7$. The artificial broadening $\gamma = 10^{-2}$ was applied.

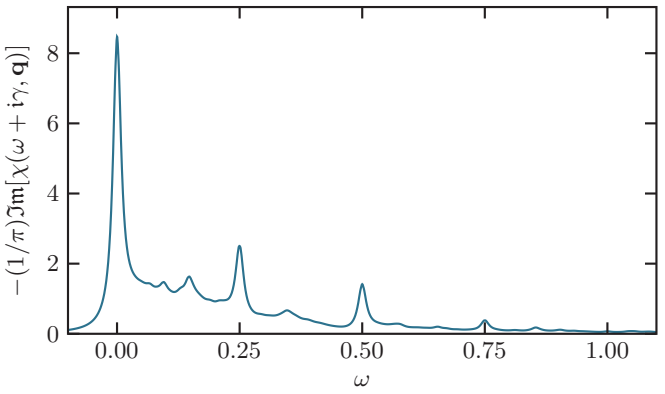

FIG. 6. Spin-wave spectrum for a random two-dimensional MNA, the wave vector $(0.25,0,0)2\pi/a$, and the concentration $c = 0.4$ below the percolation threshold. The artificial broadening $\gamma = 10^{-2}$ was applied.

more pronounced in the systems with lower dimension. For the 1D case, it vanishes only in the limit of perfect structure. Such a behavior is explained by the increased probability of forming the isolated islands in systems with lower dimension. Second, as mentioned above, in two and three dimensions the peak survives also above the percolation threshold, though with decreasing weight.

Further insight is gained by analyzing the distribution of the spectral density in the reciprocal space, cf. Fig. 8, the so-called constant-energy scans. The reference energy zero, corresponding to the Goldstone mode, allows a particularly clear interpretation. The figure depicts the distribution of the Goldstone mode in the reciprocal space along the (100) direction. We clearly observe that the Goldstone mode becomes more localized in the real space (delocalized in the reciprocal space) as the concentration decreases. Figure 8(b) shows that the localization is more pronounced in systems with the reduced dimensionality.

B. Performance of the CPA

As we have seen in the previous section, even the simplified model of MNAs features rich physics of SE dynamics. We recall that the Monte Carlo simulations yield numerically exact results. Now, we address the question of how far the physics of the SE can be captured within the coherent-potential approximation.

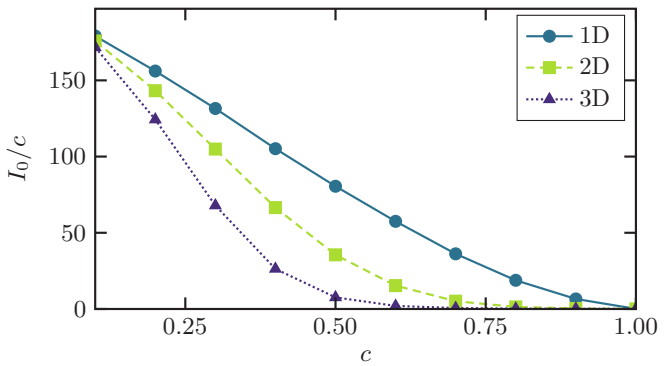

FIG. 7. The normalized intensity $I_0(c)/c$ of the zero-energy peak in the spin-wave spectra for the wave vector $(0.25,0,0)2\pi/a$ in different dimensions as a function of concentration.

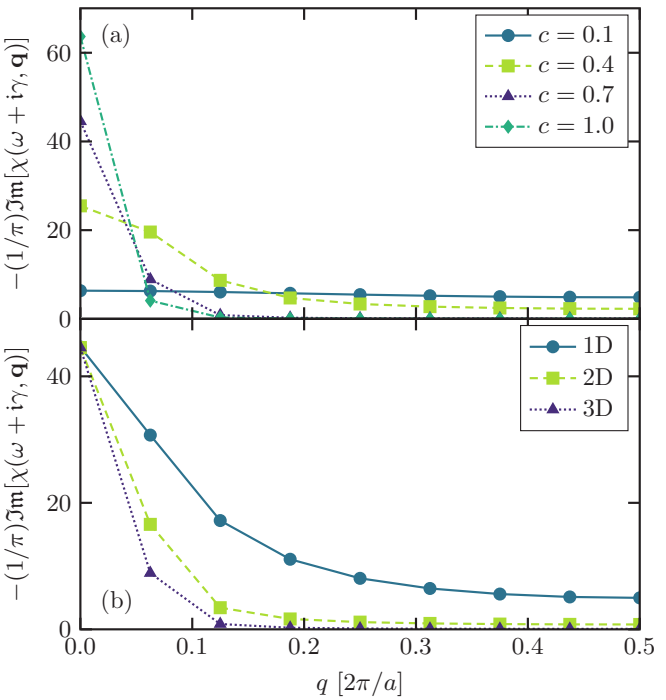

FIG. 8. The intensity of the Goldstone mode for different dimensionality, concentrations, and wave vectors along (100) direction. The figures represent constant-energy scans for zero energy and thus the distribution of the Goldstone mode in the Fourier space: (a) three-dimensional system at different concentrations, (b) impact of the dimensionality for concentration $c = 0.7$.

Figure 9 compares the Monte Carlo and the coherent-potential approximation results for a disordered nanowire. We clearly see that the CPA is unable to reproduce the series of sharp SE resonances yielding a continuum of states instead. The qualitative failure of CPA stems from its mean-field character and as such CPA cannot account for the details of the

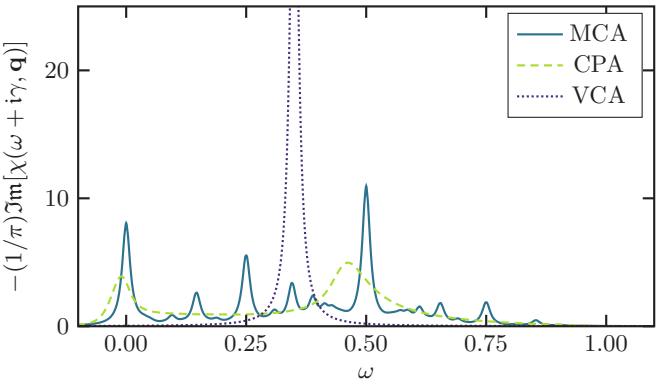

FIG. 9. Comparison of spin-wave spectra from Monte Carlo, CPA, and virtual-crystal approximation. The spectra correspond to a random MNA in one dimension, the wave vector $(0.25,0,0)2\pi/a$, and the concentration $c = 0.7$. The artificial broadening $\gamma = 10^{-2}$ is applied.

disordered local atomic environment leading to the formation of islands supporting the local SE modes. It is interesting to analyze the origin of the zero-energy peak in Fig. 9 in the CPA spectrum. In one dimension, the density of states $[\mathrm{Im}\mathcal{G}(\mathbf{R}=\mathbf{0},\omega+\mathrm{i}0^{+})]$ diverges for small energies as $\omega^{-1/2}$. The behavior is reflected also in the imaginary part of the magnetic weight $\mathcal{W}$ leading to the enhanced imaginary part of the susceptibility in the limit of small ω. Thus, this feature is absent in the case of two- and three-dimensional systems, where the density of states is nonsingular at small energies. On the other hand, the peak at higher energies stems from a pole of the magnon propagator $\mathcal{G}$ corresponding to the value of the self-energy; cf. Fig. 20(c).

A careful inspection of the low-energy CPA spectrum shows a small shift of the spectral weight to the region of negative energies. This is an artifact of the method that results from the poor performance of the CPA in one dimension and the difficulty of performing a precise analytic continuation of the strongly asymmetric peak. In two and three dimensions, this problem does not appear. However, the tail of the peak, reaching towards the region of negative energies, will appear in all dimensions as it is a result of the artificial broadening γ.

The CPA performs much more satisfactorily in higher dimensions above the percolation threshold, cf. Fig. 10, yielding spectra resembling closely the Monte Carlo results. The success points to the fact that the local details of the atomic environment become less important in higher dimensions due to the larger number of nearest neighbors and a better connectivity of the random magnetic system.

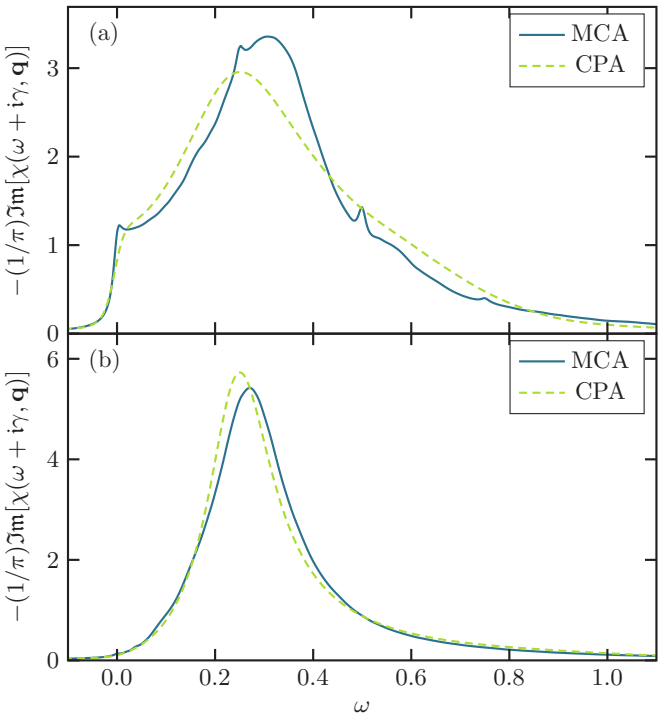

FIG. 10. Comparison of Monte Carlo and CPA spin-wave spectra in (a) two and (b) three dimensions. The spectra correspond to the wave vector $(0.25,0,0)2\pi/a$, and the concentration $c=0.7$. The artificial broadening $\gamma=10^{-2}$ is applied.

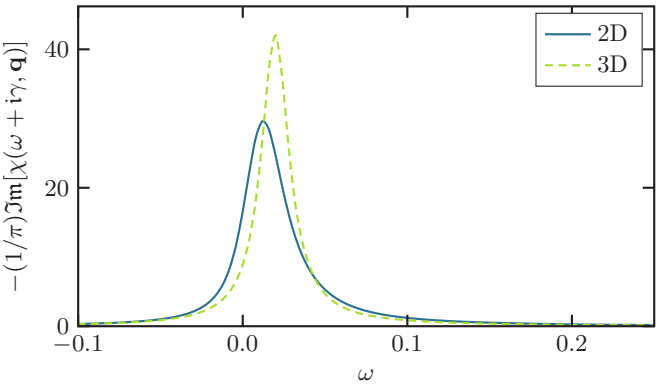

FIG. 11. Spin-wave spectra from MCA for a random MNA in two and three dimensions, the wave vector $(0.0625,0,0)2\pi/a$, and the concentration $c=0.7$. The artificial broadening $\gamma=10^{-2}$ is applied.

We note that the virtual-crystal approximation fails completely and yields just a single infinitely long-living magnon mode. The reason for that is the essentially static character of the VCA self-energy. Furthermore, as we will see below, the VCA is insensitive to the dimensionality of the magnetic system.

C. Long-wavelength behavior

The discussion in Sec. III A made clear that while in the one-dimensional case the spectra are dominated by the localized SE, in two and three dimensions and at higher concentrations one can expect well-formed spin-wave peaks. As evident from Fig. 11 the spin-wave peaks for wave vectors close to the center of the Brillouin zone assume regular Lorentzian shapes. It is therefore reasonable to investigate how the energy of the peak (the position of the maximum, ω_q) and its full width at half maximum (FWHM) depend on the wave vector and the concentration. Our calculations show that ω_q grows quadratically with q for small wave vectors and the proportionality parameter is called stiffness constant D. As shown in Fig. 12, both the stiffness constant and FWHM are dimensionality and concentration dependent.

We note that the definition of the "spin-wave quasiparticle" is less straightforward close to the percolation threshold; cf., e.g., Fig. 4(c). The peaks feature a clear asymmetry, which is caused by the overlap of the "spin-wave-type peak" at nonzero energy and the zero-energy peak of the Goldstone mode of the isolated clusters.

Figure 12(a) shows that in any dimension the function $D(c)$ deviates strongly from the simple linear dependence predicted by the VCA. The deviation and damping [cf. Fig. 12(b)] are larger in two than in three dimensions. The latter trend follows from the smaller coordination numbers of the two-dimensional lattice, where the nonstoichiometry and disorder more strongly influence the neighborhood of the given magnetic moment. The stiffness constant tends to zero around the percolation threshold. The vanishing of the stiffness constant means that the position of the maximum of the low-energy peak does not vary with the wave vector and remains zero for all $\mathbf{q}$'s. We note that CPA accounts well for the dependence of the stiffness parameter and FWHM on c and their dimensionality trends. Its

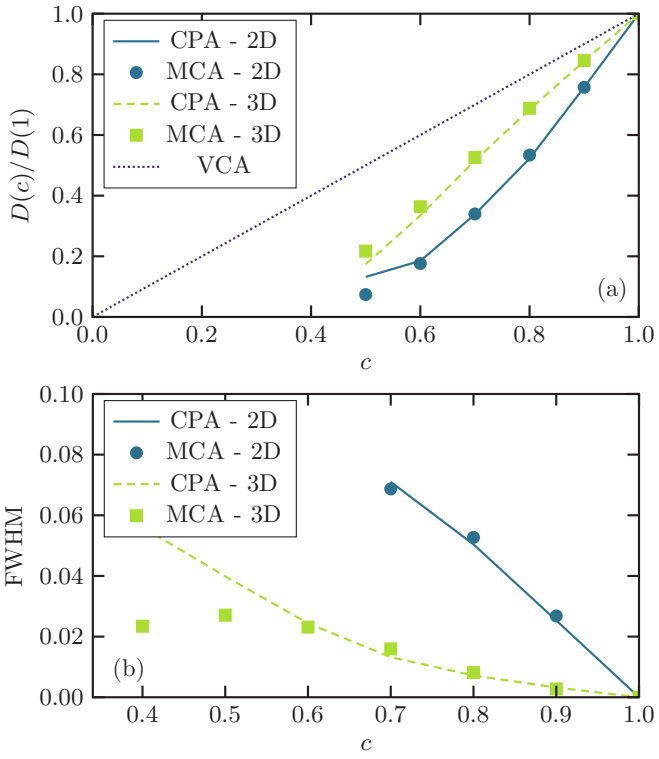

FIG. 12. (a) Spin-wave stiffness constant D normalized to the perfect magnet value of 0.25 and (b) FWHM for the wave vector $(0.125,0,0)2\pi/a$ for our model of MNA in two and three dimensions as a function of concentration c. Solid lines represent CPA results while point corresponds to the Monte Carlo simulations (2D, ●; 3D, ■). In (a) the VCA result is a simple straight line independent of the dimensionality. VCA yields magnons with infinite lifetimes (zero FWHM) for any concentration.

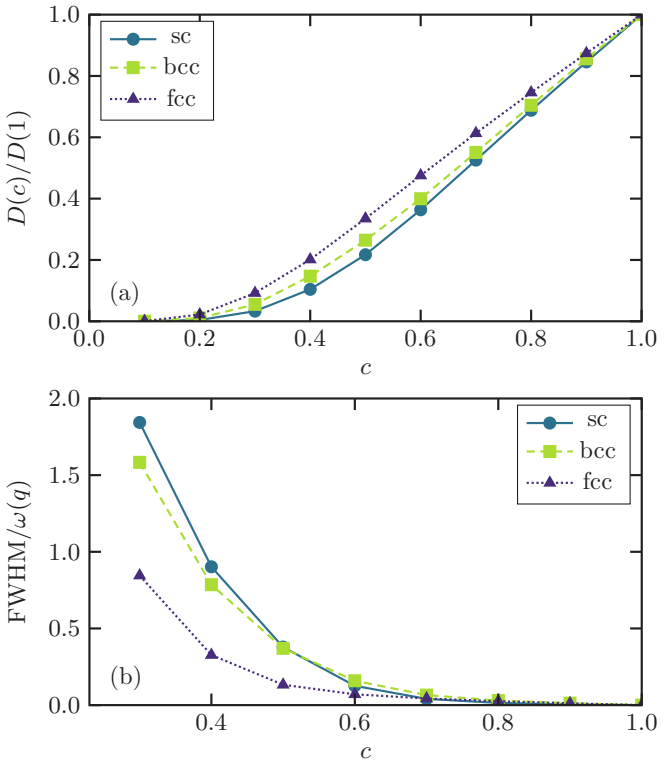

FIG. 13. (a) Spin-wave stiffness constant D normalized to the perfect magnet value of 0.25 as a function of concentration for three cubic Bravais lattices: simple cubic (sc), body-centered cubic, and face-centered cubic (fcc). (b) The corresponding FWHM for the wave vector $(0.125,0,0)2\pi/a$ normalized to the peak position at this wave vector. The results are based on the Monte Carlo simulations.

performance is clearly less satisfactory in the case of FWHM in the vicinity of the percolation threshold. It is a hint that the damping is controlled by the local properties of the disordered environment, which are necessarily poorly represented within the mean-field CPA theory.

Finally, we compare the long-wavelength SE properties of three cubic lattices: simple cubic, body-centered cubic, and face-centered cubic; cf. Fig. 13. One can again clearly notice that the disorder influences the lattices with small coordination numbers more seriously. Concerning the spin-wave stiffness constant, it tends to zero faster for structures with smaller number of nearest neighbors. Furthermore, the damping increases with the decreasing number of nearest neighbors.

IV. IMPACT OF THE ELECTRONIC STRUCTURE

In the previous sections we took a careful look at the evolution of spin-wave energies and lifetimes in model systems, in which the exchange parameters and magnetic moments are not altered by the presence of impurities. In real systems this assumption does not in general hold since the alloying changes the electronic structure and thus the magnetic properties. While the effect is necessarily system dependent, it is instructive to consider a particular example.

While the ultrastrong low-density steels based on FeAl enjoy recently renewed attention [11], the spin dynamics of this system has not been studied so far. We consider Fe_cAl_{1-c} at low and moderate Al concentrations and 0 K. In three dimensions and for concentrations of Al $1-c<0.30$, the system is regarded as a substitutionally random alloy in the sense defined in Sec. II B. Its magnetic and structure phase diagram is complex but in the regime considered here FeAl features bcc lattice structure and ferromagnetic ordering [37,38]. The lattice constant was determined to expand linearly with growing Al content [39]. Much less is known about the structure and magnetism of thin FeAl films and nanostructures. To allow the comparison with the three-dimensional counterpart, we consider a single free (100) layer of uncorrelated FeAl alloy with lattice constant of bcc Fe independent of Al concentration.

The ground state of the alloy was determined based on the local density approximation and the CPA for the electron subsystem. Figure 14 depicts the dependence of the average magnetic moment on Fe sites in Fe_cAl_{1-c} as a function of concentration c. The value does not considerably vary. We also note the enhanced value of the moment in the freestanding film. The exchange parameters are evaluated using the magnetic force theorem as implemented with the multiple scattering theory [40] and taking advantage of the vertex cancellation theorem in the disordered case [41,42]. They are presented in Fig. 15. We note the RKKY oscillatory

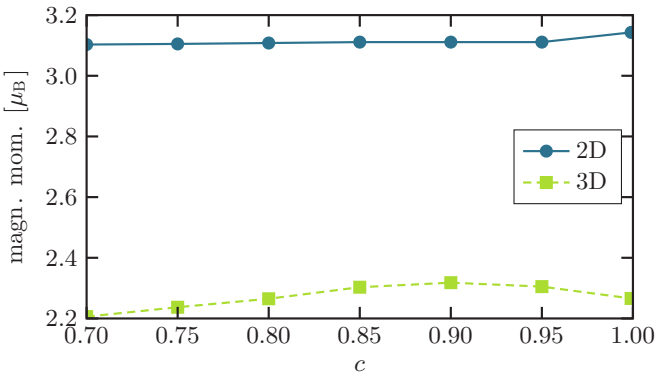

FIG. 14. The dependence of the average magnetic moment on Fe site in Fe_cAl_{1-c} as a function of concentration c.

character of the parameters, which gradually disappears in the disordered phase. The second-nearest-neighbor interaction is not negligible but more pronounced in the bulk case. While in the film the parameters vary weakly with the concentration, in three dimensions the exchange parameters between first nearest neighbors grow with the Al concentration in the considered regime, while those between second nearest neighbors decrease.

The SEs presented in this section were obtained using the Monte Carlo approach. In the long-wavelength regime the SEs in Fe_cAl_{1-c} behave in a considerably more complex way than the one given by the simple models studied earlier in this paper; cf. Fig. 16(a). In two dimensions, the spin-wave stiffness decreases with the Fe concentration, however slightly

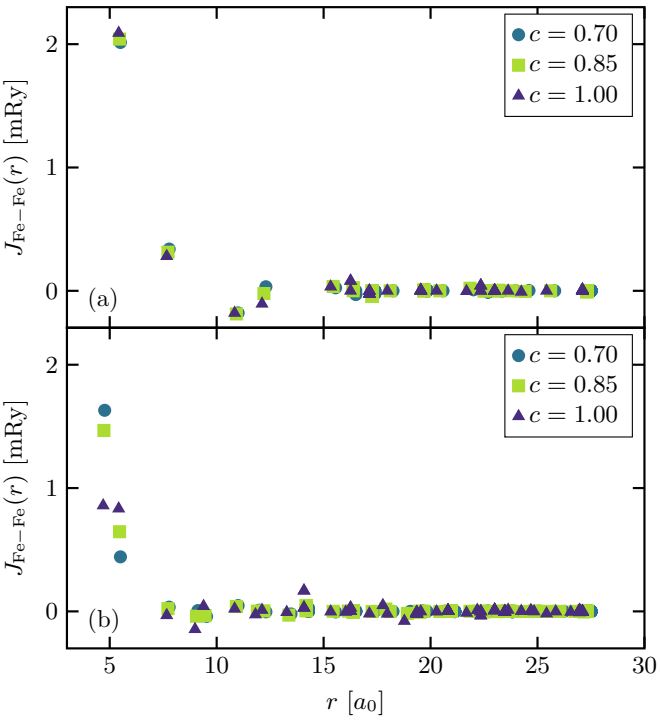

FIG. 15. The exchange parameters between Fe moments in Fe_cAl_{1-c} as a function of concentration c in (a) two and (b) three dimensions.

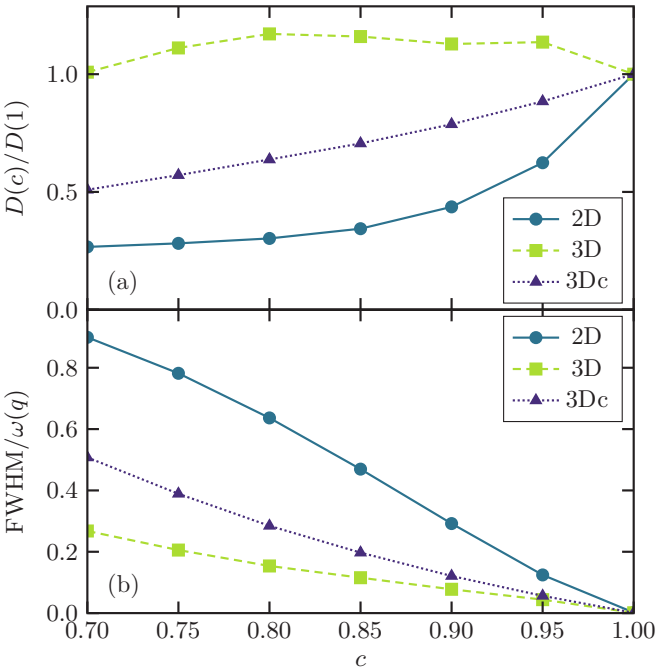

FIG. 16. (a) The normalized spin-wave stiffness constant and (b) the normalized FWHM at $q = (0.125,0,0)2\pi/a$ for Fe_cAl_{1-c} as a function of concentration c for two dimensions (2D), three dimensions (3D), and three dimensions with exchange parameters kept constant and taken from the $c = 1$ case (3Dc).

faster than in the simple model considered in Sec. III C. The difference in the trend is caused by the long-ranged character of the exchange parameters and the fact that they become antiferromagnetic at the 3rd and 4th neighbor shell. The random removal of the magnetic atoms influences more strongly the less numerous ferromagnetic nearest- and next-nearest-neighbor shells than the more numerous further antiferromagnetic shells. In three dimensions, it initially increases reaching maximum around $c = 0.8$. The origin of this effect is the increase of the nearest-neighbor exchange parameters with the rise of Al concentration. The decrease of the next-nearest-neighbor exchange parameters is weaker and cannot fully compensate for this trend. Additionally, the Al doping weakens the antiferromagnetic coupling seen at further shells. In three dimensions, we performed one more set of calculations, in which the exchange parameters were kept constant and taken from the $c = 1$ case. The spin-wave stiffness constant decreases in this case almost as predicted in the simple model disregarding the farther than first neighbors. The reason for this is the fact that the first and the second shells with the almost equal number of members (8 and 6, respectively) are similarly affected by the disorder.

We remark that in general the long-range ferromagnetic exchange interactions are expected to soften the decrease of the spin-wave stiffness constant with the concentration. The farther shells involve more atoms and as such are less sensitive to the introduction of the nonmagnetic vacancies.

The normalized FWHM of the spin-wave modes depicted in Fig. 16(b) follows the trend similar to the one observed in Sec. III C. The FWHM increases with the increasing impurity

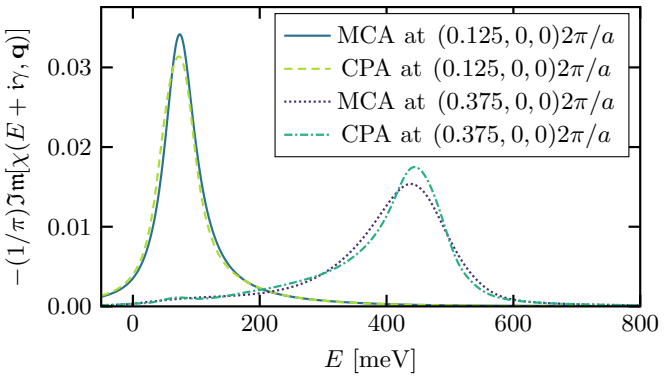

FIG. 17. Comparison of MCA and CPA spin-wave spectra for Fe_cAl_{1-c} with concentration $c = 0.7$. The spectra correspond to the wave vectors $(0.125,0,0)2\pi/a$ and $(0.375,0,0)2\pi/a$. The artificial broadening $\gamma = 20$ meV is applied.

concentration and the effect is more pronounced for lower dimensionality. However, it can be clearly seen that the long-range character of the exchange parameters plays an important role here, as evident from the comparison of the cases with exchange parameters varying with the concentration and independent of it.

Finally, we compared the performance of the CPA for the three-dimensional Fe_cAl_{1-c} alloy for $c = 0.7$ with the results of the Monte Carlo calculations (see Fig. 17). The results show very good agreement, especially for smaller wave vectors. For larger wave vectors, minor differences appear in the spectrum. However, the size, position, and width of the main peak is still in good agreement.

V. SUMMARY AND DISCUSSION

The SEs of low-dimensional disordered magnets feature a remarkably rich physics. In the case of MNAs with uncorrelated disorder one can distinguish two regimes. In the case of low concentration of magnetic atoms the SE spectra are dominated by localized (standing) SE modes confined to single atoms or small clusters. As the concentration of the magnetic atoms increases, the system becomes dominated by large connected clusters and the extended spin-wave states emerge. They manifest themselves as well-defined Lorentzian peaks of a finite width in the imaginary part of the Fourier transformation of the magnetic susceptibility. The states can be pictured as Bloch waves with a finite lifetime arising from the scattering on the crystal imperfections.

The crossover between the low and high concentration regimes is by no means sharp. Even above the percolation threshold (i.e., for high concentrations of magnetic atoms) small detached clusters of atoms can form, giving rise to sharp SE modes in addition to the continuum spectra of the spin-wave modes. On the other hand, large connected clusters of atoms can appear also below the threshold supporting multiple SE modes with practically continuous energy spectrum. In the case of magnets with long-range exchange interactions the crossover is expected to be even less pronounced.

Taking the width of the well-defined magnon peaks as a measure of the disorder impact (in the perfect case they feature no intrinsic width), one arrives at the conclusion that the low-dimensional magnets are more strongly affected by nonstoichiometry and disorder then their bulk counterparts. This behavior follows from the smaller coordination number of atoms in the thin films and wires than in the bulk: the local environment of a magnetic moment is more strongly disturbed by the disorder in smaller dimensions. A similar trend can be seen in bulk phases with different coordination numbers. On the other hand, as the study of FeAl shows, the details of this dependence might be altered by the long-range character of the exchange interactions.

The coherent-potential approximation provides a remarkably good description of the magnon excitations for high concentrations of magnetic atoms in two and three dimensions, including the actual dimensionality trends. However, due to its mean-field character, it is unable to predict the emergence of standing SE modes localized on the detached clusters of atoms. The CPA performance is better in the case of the spin-wave dispersion than in the case of their widths, which suggests that the latter are controlled by the details of local random configurations of atoms, which cannot be grasped by the CPA. The virtual-crystal approximation fails qualitatively in the description of disordered magnets; in particular it cannot account for the finite width of the spin-wave peaks. Furthermore, the VCA results are not dimensionality dependent.

There are a number of natural extensions to this work. Among them are the study of the impact of the correlated disorder and first-principles study of the spin excitations in the alloys containing several magnetic atoms. These studies must be the topics of separate publications.

ACKNOWLEDGMENTS

P.B. acknowledges the generous support of the Alexander von Humboldt Foundation during his stay as a Feodor Lynen Research Fellow at the University of Missouri–Columbia, USA. This work is supported by the Deutsche Forschungsgemeinschaft under Grant No. ER 340/5-2 and the Joint Initiative for Research and Innovation within the Fraunhofer and the Max Planck society cooperation program.

APPENDIX: CPA FOR THE HEISENBERG HAMILTONIAN

The coherent-potential approximation for the transverse magnetic susceptibility of the Heisenberg Hamiltonian is constructed as follows. We define the *species-resolved Fourier transformation of the susceptibility*

$$\chi_{ij}^{\alpha\beta}(\mathbf{q},\mathbf{q}') = \sum_{\mathbf{R}\mathbf{R}'} p^{\alpha i}(\mathbf{R}) e^{-i\mathbf{q}\cdot\mathbf{R}} \chi(\mathbf{R}+\mathbf{s}_i,\mathbf{R}'+\mathbf{s}_j) p^{\beta j}(\mathbf{R}') e^{i\mathbf{q}'\cdot\mathbf{R}'}, \tag{A1}$$

which allows us to compute the Fourier transform of the full susceptibility as

$$\chi_{ij}(\mathbf{q},\mathbf{q}') = \sum_{\alpha\beta} \chi_{ij}^{\alpha\beta}(\mathbf{q},\mathbf{q}'). \tag{A2}$$

The susceptibility $\chi(z,\mathbf{q},\mathbf{q}')$ corresponds to a single random configuration of the atoms constituting the alloy.

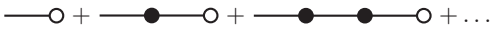

FIG. 18. Expansion of the $\chi_{ij}^{\alpha\beta}(z,\mathbf{q},\mathbf{q}')$ susceptibility.

Following Eq. (5) the susceptibility in the real space can be developed in a formal series

$$\chi(z) = G_0 g S + G_0 g S T G_0 g S + G_0 g S T G_0 g S T G_0 g S + \cdots, \tag{A3}$$

where the ST product is given by Eq. (6).

The Fourier transformation $\chi_{ij}^{\alpha\beta}(z,\mathbf{q},\mathbf{q}')$ can be computed term-by-term upon a series of tedious algebraic manipulations and has the diagrammatic representation depicted in Fig. 18. The diagram consists of three elements listed below. Each of the elements is a matrix in a space of composite indices involving basis sites and atomic species. The following notation is used: $(i) \equiv i\alpha, (j) \equiv j\beta, (l) \equiv l\gamma, (m) \equiv m\mu$, etc. Furthermore, in this index space the Einstein summation convention is used. The elements are

(1) $\mathcal{T}$ matrix denoted with filled circle (•):

$$\mathcal{T}_{ij}^{\alpha\beta}(\mathbf{q},\mathbf{q}') = \rho^{(l)}(\mathbf{q}-\mathbf{q}')\tau_{(i)(j)}^{(l)}(\mathbf{q},\mathbf{q}'), \tag{A4}$$

where

$$\tau_{(i)(j)}^{(l)}(\mathbf{q},\mathbf{q}') \equiv g S_\beta^{-1}\left(J_{jl}^{\beta\gamma}(\mathbf{q}-\mathbf{q}')\delta_{(i)(j)} - J_{lj}^{\gamma\beta}(\mathbf{q}')\delta_{(i)(l)}\right), \tag{A5}$$

$$\rho^{\alpha i}(\mathbf{q}) \equiv \sum_{\mathbf{R}} p^{\alpha i}(\mathbf{R})\mathfrak{e}^{-i\mathbf{q}\cdot\mathbf{R}}, \tag{A6}$$

$$J_{ij}^{\alpha\beta}(\mathbf{q}) \equiv \sum_{\mathbf{R}} J_{ij}^{\alpha\beta}(\mathbf{R})\mathfrak{e}^{-i\mathbf{q}\cdot\mathbf{R}}. \tag{A7}$$

The two latter quantities are lattice Fourier transformations of the occupation function and the exchange parameters, respectively.

(2) $\mathcal{S}$ matrix denoted with open circle (○):

$$\mathcal{S}_{(i)(j)}(\mathbf{q},\mathbf{q}') = \rho^{(l)}(\mathbf{q}-\mathbf{q}')\sigma_{(i)(j)}^{(l)}, \tag{A8}$$

$$\sigma_{(i)(j)}^{(l)} \equiv g\delta_{(i)(j)}\delta_{(i)(l)}S_{(l)}. \tag{A9}$$

(3) Propagator of uncoupled magnetic moments (———):

$$\Gamma_{(i)(j)}(z) = z^{-1}\delta_{(i)(j)}. \tag{A10}$$

This matrix does not depend on the momentum but introduces the frequency dependence into the equations.

The rules for evaluating the diagrams are as follows:

(1) The matrices in the $(i)(j)$ space brought together in a diagram undergo the matrix multiplication in this space.

(2) Every internal free propagator line is associated with an integration over a Brillouin zone, denoted as

$$\frac{1}{\Omega_{\mathrm{BZ}}}\int_{\mathbf{q}\in\Omega_{\mathrm{BZ}}} f(\mathbf{q})\mathrm{d}\mathbf{q} \equiv \int_{\mathbf{q}} f(\mathbf{q}) \tag{A11}$$

in order to simplify the notation.

For instance, the second term, i.e., including the product of two random variables $\rho^{(i)}(\mathbf{q})$, in the expansion presented in Fig. 18 is explicitly written as

$$\chi_{ij}^{\alpha\beta}(z,\mathbf{q},\mathbf{q}') = z^{-2}\int_{\mathbf{q}_1} \mathcal{T}_{(i)(m_1)}(\mathbf{q},\mathbf{q}_1)\mathcal{S}_{(m_1)(j)}(\mathbf{q}_1,\mathbf{q}')$$
$$\text{(2nd order)} \tag{A12}$$
$$= z^{-2}\int_{\mathbf{q}_1} \rho^{(l_1)}(\mathbf{q}-\mathbf{q}_1)\tau_{(i)(m)}^{(l_1)}(\mathbf{q},\mathbf{q}_1) \times \rho^{(l_2)}(\mathbf{q}_1-\mathbf{q}')\sigma_{(m)(j)}^{(l_2)}. \tag{A13}$$

[Note the Einstein convention for the indices (l_1),(l_2), and (m).]

In the next step, our goal is to compute the averaged susceptibility. As stated in Sec. II C, upon the averaging, the translational symmetry of the system is restored and the susceptibility depends only on one wave-vector variable,

$$\left\langle\chi_{ij}^{\alpha\beta}(z,\mathbf{q},\mathbf{q}')\right\rangle \equiv \left\langle\chi_{ij}^{\alpha\beta}(z,\mathbf{q})\right\rangle\Omega_{\mathrm{BZ}}\delta(\mathbf{q}-\mathbf{q}'). \tag{A14}$$

In what follows, we will construct the coherent-potential approximation for $\langle\chi_{ij}^{\alpha\beta}(z,\mathbf{q})\rangle$. We attempt to average every term of the expansion presented in Fig. 18 separately and following Yonezawa [32] we resort to the so-called cumulant expansion. As an example, let us consider again the 2nd order term given in Eq. (A13):

$$\left\langle\chi_{ij}^{\alpha\beta}(z,\mathbf{q},\mathbf{q}')\right\rangle = z^{-2}\int_{\mathbf{q}_1} \tau_{(i)(m)}^{(l_1)}(\mathbf{q},\mathbf{q}_1)\sigma_{(m)(j)}^{(l_2)} \times \langle\rho^{(l_1)}(\mathbf{q}-\mathbf{q}_1)\rho^{(l_2)}(\mathbf{q}_1-\mathbf{q}')\rangle. \tag{A15}$$

We note that only the ρ functions contain random variables p and require averaging. The cumulant expansion of the product reads

$$\langle\rho^{(l_1)}(\mathbf{k}_1)\rho^{(l_2)}(\mathbf{k}_2)\rangle = \mathcal{C}^2_{(l_1)(l_2)}(\mathbf{k}_1,\mathbf{k}_2) + \mathcal{C}^1_{(l_1)}(\mathbf{k}_1)\mathcal{C}^1_{(l_2)}(\mathbf{k}_2), \tag{A16}$$

where $\mathcal{C}^n$ stands for the multivariate cumulant of order n. In the case of the uncorrelated disorder

$$\mathcal{C}^n_{(l_1)(l_2)\ldots(l_n)}(\mathbf{k}_1,\mathbf{k}_2,\ldots,\mathbf{k}_n) = \mathcal{P}^n_{(l_1)(l_2)\ldots(l_n)}(\mathfrak{c})\Omega_{\mathrm{BZ}} \times \delta(\mathbf{k}_1+\mathbf{k}_2+\cdots+\mathbf{k}_n), \tag{A17}$$

where $\mathfrak{c}$ is the concentration matrix $c_{i\alpha}$. The weight functions $\mathcal{P}$ in the uncorrelated case are nonzero only if all indices correspond to the same basis site. They do not have any straightforward analytic representation but the first two read

$$\mathcal{P}^1_{i\alpha}(\mathfrak{c}) = c_{i\alpha}, \tag{A18}$$

$$\mathcal{P}^2_{i\alpha j\beta}(\mathfrak{c}) = \delta_{ij}(\delta_{\alpha\beta}c_{i\alpha} - c_{i\alpha}c_{j\beta}). \tag{A19}$$

The momentum dependence of the cumulants gives, as expected from Eq. (A14), that the averaged susceptibility is diagonal in the momentum arguments and thus proportional to $\Omega_{\mathrm{BZ}}\delta(\mathbf{q}-\mathbf{q}')$.

Examples of the cumulant expansion for the second and fourth order terms are presented in Fig. 19. The coherent-potential approximation neglects the terms involving multiple "crossed" cumulants. The lowest order term of this type appears in the 4th order average and is marked with (†) in Fig. 19.

In the CPA, the final expression for the averaged diagonal part $\langle\chi_{ij}^{\alpha\beta}(z,\mathbf{q})\rangle$ of the susceptibility, cf. Eq. (A14), is constructed by summing the terms of all order by means of a Dyson-like self-consistent equation. Because our diagrams feature two types of vertices, namely $\mathcal{T}$ and $\mathcal{S}$, two quantities

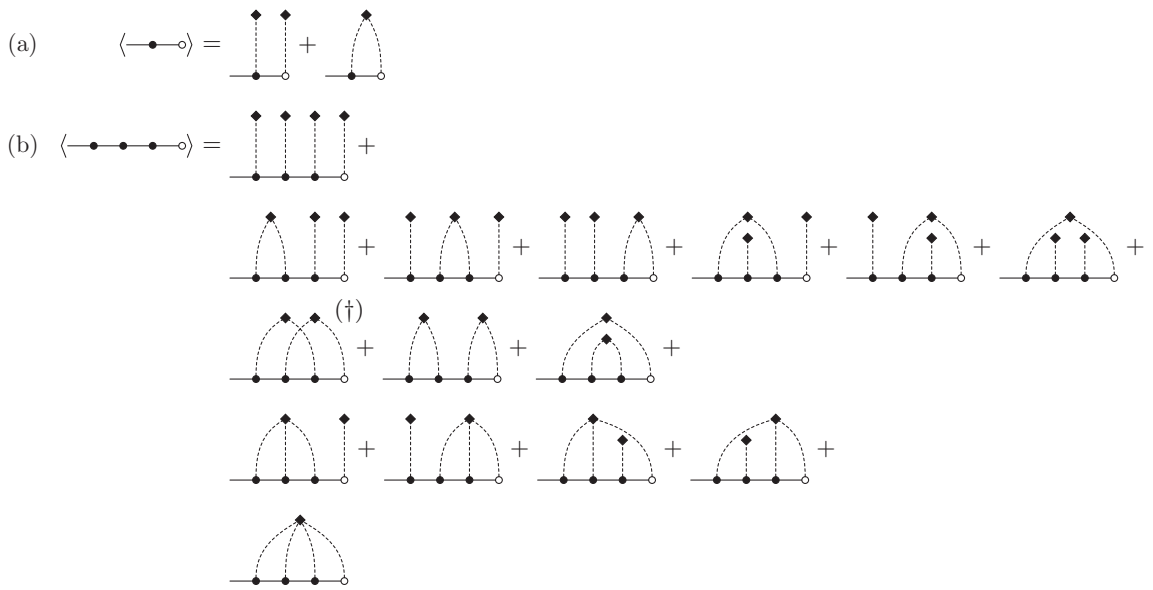

FIG. 19. Expansion of the second (a) and fourth (b) order term average. The bundles of dashed lines denote cumulants $\mathcal{C}^n$. Crossed terms, like those denoted with (†), are omitted in the coherent-potential approximation. The remaining symbols are identical to those used in Fig. 18.

appear, namely the CPA *effective medium propagator* $\mathcal{G}(z,\mathbf{q})$ and the *magnetic weight correction* $\mathcal{W}(z,\mathbf{q})$.

The propagator

$$\mathcal{G}(z,\mathbf{q}) = \Gamma(z) + \Gamma(z)\mathcal{E}(z,\mathbf{q})\mathcal{G}(z,\mathbf{q}) \tag{A20}$$

is expressed in terms of the *self-energy* $\mathcal{E}$,

$$\begin{aligned}\mathcal{E}(z,\mathbf{q}) = \sum_{s\in S_1} \mathcal{P}_s^1 \tau^{(l_1)}(\mathbf{q},\mathbf{q}) + \sum_{n=2}^{\infty}\sum_{s\in S_n} \mathcal{P}_s^n \int_{\mathbf{q}_1}\int_{\mathbf{q}_2} \\ \cdots \int_{\mathbf{q}_{n-1}} [\tau^{(l_1)}(\mathbf{q},\mathbf{q}_1)\mathcal{G}(z,\mathbf{q}_1)\tau^{(l_2)}(\mathbf{q}_1,\mathbf{q}_2)\mathcal{G}(z,\mathbf{q}_2)\cdots \\ \cdots \tau^{(l_{n-1})}(\mathbf{q}_{n-2},\mathbf{q}_{n-1})\mathcal{G}(z,\mathbf{q}_{n-1})\tau^{(l_n)}(\mathbf{q}_{n-1},\mathbf{q})],\end{aligned} \tag{A21}$$

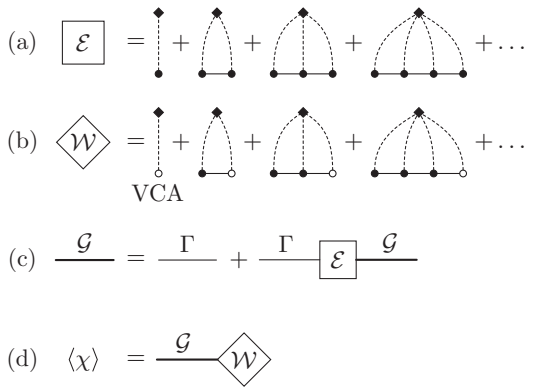

FIG. 20. The diagrammatic representation of the Dyson equation for the CPA susceptibility: expansions of the CPA self-energy (a) and the magnetic weight (b) given by Eqs. (A21) and (A22), respectively, (c) the Dyson equation (A20), and (d) the final expression for the averaged susceptibility corresponding to Eq. (A23). Restricting the series in (a) and (b) to the first terms only yields the virtual-crystal approximation.

where $S_n \ni s = \{(l_1),(l_2),\ldots,(l_n)\}$ is a particular length n sequence of composite indices. Similarly, the weight correction $\mathcal{W}$ amounts to

$$\begin{aligned}\mathcal{W}(z,\mathbf{q}) = \sum_{s\in S_1} \mathcal{P}_s^1 \sigma^{(l_1)} + \sum_{n=2}^{\infty}\sum_{s\in S_n} \mathcal{P}_s^n \int_{\mathbf{q}_1}\int_{\mathbf{q}_2} \\ \cdots \int_{\mathbf{q}_{n-1}} [\tau^{(l_1)}(\mathbf{q},\mathbf{q}_1)\mathcal{G}(z,\mathbf{q}_1)\tau^{(l_2)}(\mathbf{q}_1,\mathbf{q}_2)\mathcal{G}(z,\mathbf{q}_2)\cdots \\ \cdots \mathcal{G}(z,\mathbf{q}_{n-1})\sigma^{(l_n)}].\end{aligned} \tag{A22}$$

The final expression for the averaged susceptibility involves the matrix product of the effective propagator and the weight correction

$$\langle\chi(z,\mathbf{q})\rangle = \mathcal{G}(z,\mathbf{q})\mathcal{W}(z,\mathbf{q}). \tag{A23}$$

The expansion presented above is depicted in terms of diagrams in Fig. 20. The calculation process involves self-consistency, as the effective medium propagator $\mathcal{G}$ is found using the self-energy $\mathcal{E}$, which in turn involves the propagator.

The series given by Eqs. (A21) and (A22) do not converge term-by-term. Furthermore, it is computationally unfeasible to work directly in the reciprocal space. Below, we transform the corresponding quantities to the real-space representation, where we sum over the series. For simplicity the frequency arguments are suppressed.

$$\mathcal{E}(\mathbf{q}) = \mathcal{E}(\mathbf{q},\mathbf{q}) \equiv \sum_{\mathbf{R}\mathbf{R}'} \mathfrak{e}^{-\mathbf{q}\cdot(\mathbf{R}-\mathbf{R}')}\mathcal{E}(\mathbf{R},\mathbf{R}'), \tag{A24}$$

$$\mathcal{W}(\mathbf{q}) \equiv \sum_{\mathbf{R}} \mathfrak{e}^{-\mathbf{q}\cdot\mathbf{R}}\mathcal{W}(\mathbf{R}), \tag{A25}$$

$$\mathcal{E}(\mathbf{R},\mathbf{R}') = \sum_{i\alpha} c_{i\alpha} \sum_{\mathbf{R}_1} \hat{\mathcal{E}}^{i\alpha}(\mathbf{R},\mathbf{R}_1)\tau^{i\alpha}(\mathbf{R}_1,\mathbf{R}'), \tag{A26}$$

$$\mathcal{W}(\mathbf{R}) = \sum_{i\alpha} c_{i\alpha}\hat{\mathcal{E}}^{i\alpha}(\mathbf{R},\mathbf{0})\sigma^{\alpha i}. \tag{A27}$$

The *partial self-energies* $\hat{\mathcal{E}}$ are determined as follows:

$$\bar{\mathcal{E}}^i(\mathbf{R},\mathbf{R}') = \sum_{\alpha\in I_i}\sum_{\mathbf{R}_1} c_{i\alpha}\hat{\mathcal{E}}^{i\alpha}(\mathbf{R},\mathbf{R}_1)\mathcal{M}^{i\alpha}(\mathbf{R}_1,\mathbf{R}'), \tag{A28}$$

where I_i denotes the set of impurity types present on site i. The terms off-diagonal in the sites' space are zero in the case of uncorrelated disorder. In what follows, we will work with matrices in a space of extended composite indices including both the composite index (i) as well as the lattice vector $\mathbf{R}$, i.e., $(\alpha i\mathbf{R})$. It is sufficient to consider only finite clusters of lattice vectors corresponding to the range of the exchange parameters $J(\mathbf{R})$. Using the concept of the effective interaction of Yonezawa the summation of the cumulant series yields

$$c_{i\alpha}\hat{\mathcal{E}}^{i\alpha} = \mathcal{P}^1_{i\alpha}\mathsf{I} + \mathcal{P}^2_{i\beta,i\alpha}\mathcal{M}^{i\beta} + \mathcal{P}^3_{i\gamma,i\beta,i\alpha}\mathcal{M}^{i\gamma}\mathcal{M}^{i\beta} + \cdots, \tag{A29}$$

$$\hat{\mathcal{E}}^{i\alpha} = [\mathsf{I} - (\mathcal{M}^{i\alpha} - \bar{\mathcal{E}}^i)]^{-1}, \tag{A30}$$

where the $\mathcal{M}$ matrices are defined in the reciprocal space by

$$\mathcal{M}^{(l)}_{(i)(j)}(\mathbf{q},\mathbf{q}') = \tau^{(l)}_{(i)(m)}(\mathbf{q},\mathbf{q}')\mathcal{G}_{(m)(j)}(\mathbf{q}') \tag{A31}$$

and in the real space consist of two parts:

$$\begin{aligned}\mathcal{M}^{(l)}_{(i)(j)}(\mathbf{R},\mathbf{R}') &= gS^{-1}_{\alpha}J^{\alpha\gamma}_{il}(\mathbf{R})\mathcal{G}_{(i)(j)}(\mathbf{R}-\mathbf{R}') \\ &\quad - \sum_{\mathbf{R}_1}\left[gS^{-1}_{\mu}J^{\gamma\mu}_{lm}(\mathbf{R}_1)\mathcal{G}_{(m)(j)}(\mathbf{R}_1-\mathbf{R}')\delta_{(i)(l)}\delta_{\mathbf{R}\mathbf{0}}\right].\end{aligned} \tag{A32}$$

The equations above can be directly implemented on a computer in order to find $\langle\chi\rangle$ and we conclude this section with several remarks concerning our numerical scheme. The convergence of the CPA self-consistency loop requires a suitable mixing of quantities from previous iterations and we resorted to the Broyden method in order to achieve it. Furthermore, the self-consistent loop does not converge for complex energies with small imaginary parts. To remedy the latter difficulty, we resorted to the nearly real axis method [10]. The self-consistent quantities were converged in a suitable distance away from the real axis and subsequently the self-energy $\hat{\mathcal{E}}(z)$ was analytically continued towards the real energies in order to recover the real-time dynamics of the system.

[1] A. A. Khajetoorians, S. Lounis, B. Chilian, A. T. Costa, L. Zhou, D. L. Mills, J. Wiebe, and R. Wiesendanger, Phys. Rev. Lett. **106**, 037205 (2011).

[2] T. Balashov, P. Buczek, L. Sandratskii, A. Ernst, and W. Wulfhekel, J. Phys.: Condens. Matter **26**, 394007 (2014).

[3] K. Zakeri, T.-H. Chuang, A. Ernst, L. Sandratskii, P. Buczek, J.-H. Qin, Y. Zhang, and J. Kirschner, Nat. Nanotechnol. **8**, 853 (2013).

[4] K. Zakeri, Phys. Rep. **545**, 47 (2014).

[5] H. Qin, K. Zakeri, A. Ernst, L. Sandratskii, P. Buczek, A. Marmodoro, T.-H. Chuang, Y. Zhang, and J. Kirschner, Nat. Commun. **6**, 6126 (2015).

[6] R. B. Muniz, A. T. Costa, and D. L. Mills, J. Phys.: Condens. Matter **15**, S495 (2003).

[7] P. Buczek, A. Ernst, P. Bruno, and L. M. Sandratskii, Phys. Rev. Lett. **102**, 247206 (2009).

[8] A. T. Costa, R. B. Muniz, and D. L. Mills, Phys. Rev. B **74**, 214403 (2006).

[9] P. Buczek, A. Ernst, and L. M. Sandratskii, Phys. Rev. Lett. **106**, 157204 (2011).

[10] P. Buczek, A. Ernst, and L. M. Sandratskii, Phys. Rev. B **84**, 174418 (2011).

[11] S.-H. Kim, H. Kim, and N. J. Kim, Nature (London) **518**, 77 (2015).

[12] L. M. Sandratskii and P. Bruno, Phys. Rev. B **66**, 134435 (2002).

[13] G. Bouzerar, J. Kudrnovský, L. Bergqvist, and P. Bruno, Phys. Rev. B **68**, 081203 (2003).

[14] L. Bergqvist, O. Eriksson, J. Kudrnovský, V. Drchal, A. Bergman, L. Nordström, and I. Turek, Phys. Rev. B **72**, 195210 (2005).

[15] A. Chakraborty, R. Bouzerar, S. Kettemann, and G. Bouzerar, Phys. Rev. B **85**, 014201 (2012).

[16] H. F. Ding, V. S. Stepanyuk, P. A. Ignatiev, N. N. Negulyaev, L. Niebergall, M. Wasniowska, C. L. Gao, P. Bruno, and J. Kirschner, Phys. Rev. B **76**, 033409 (2007).

[17] A. Chakraborty and G. Bouzerar, Phys. Rev. B **81**, 172406 (2010).

[18] A. Chakraborty, P. Wenk, S. Kettemann, R. Bouzerar, and G. Bouzerar, New J. Phys. **16**, 033004 (2014).

[19] G. Bouzerar, T. Ziman, and J. Kudrnovský, Phys. Rev. B **72**, 125207 (2005).

[20] A. Chakraborty, P. Wenk, and J. Schliemann, Eur. Phys. J. B **88**, 64 (2015).

[21] J. B. Staunton, J. Poulter, B. Ginatempo, E. Bruno, and D. D. Johnson, Phys. Rev. Lett. **82**, 3340 (1999).

[22] J. B. Staunton, J. Poulter, B. Ginatempo, E. Bruno, and D. D. Johnson, Phys. Rev. B **62**, 1075 (2000).

[23] S. V. Halilov, H. Eschrig, A. Y. Perlov, and P. M. Oppeneer, Phys. Rev. B **58**, 293 (1998).

[24] P. A. Buczek, Spin dynamics of complex itinerant magnets, Ph.D. thesis, Martin Luther Universität Halle-Wittenberg, 2009.

[25] T. Matsubara, Prog. Theor. Phys. Suppl. **53**, 202 (1973).

[26] J. A. Blackman, D. M. Esterling, and N. F. Berk, Phys. Rev. B **4**, 2412 (1971).

[27] F. Yonezawa, Prog. Theor. Phys. **40**, 734 (1968).

[28] A. Theumann, J. Phys. C **7**, 2328 (1974).

[29] G. Bouzerar and P. Bruno, Phys. Rev. B **66**, 014410 (2002).

[30] G. X. Tang and W. Nolting, Phys. Rev. B **73**, 024415 (2006).

[31] R. Vollmer, M. Etzkorn, P. S. A. Kumar, H. Ibach, and J. Kirschner, Phys. Rev. Lett. **91**, 147201 (2003).

[32] F. Yonezawa and K. Morigaki, Prog. Theor. Phys. Suppl. **53**, 1 (1973).
[33] Wikipedia, Percolation theory (Wikipedia, the free encyclopedia) (online; accessed 22 June 2015).
[34] M. E. J. Newman and R. M. Ziff, Phys. Rev. Lett. **85**, 4104 (2000).
[35] L. Kurzawski and K. Malarz, Rep. Math. Phys. **70**, 163 (2012).
[36] X. Xu, J. Wang, J.-P. Lv, and Y. Deng, Front. Phys. **9**, 113 (2014).
[37] P. Shukla and M. Wortis, Phys. Rev. B **21**, 159 (1980).
[38] Z. Jaglicic, S. Vrtnik, M. Feuerbacher, and J. Dolinsek, Phys. Rev. B **83**, 224427 (2011).
[39] H. Kleykamp and H. Glasbrenner, Z. Metal. **88**, 230 (1997).
[40] A. I. Liechtenstein, M. I. Katsnelson, V. P. Antropov, and V. A. Gubanov, J. Magn. Magn. Mater. **67**, 65 (1987).
[41] P. Bruno, J. Kudrnovský, V. Drchal, and I. Turek, Phys. Rev. Lett. **76**, 4254 (1996).
[42] J. Kudrnovský, V. Drchal, I. Turek, and P. Bruno, Surf. Sci. **507–510**, 567 (2002).